

Cite this: *Chem. Sci.*, 2025, **16**, 13031

All publication charges for this article have been paid for by the Royal Society of Chemistry

Received 1st November 2024
Accepted 16th June 2025

DOI: 10.1039/d4sc07395a
rsc.li/chemical-science

Machine learning photodynamics reveal intersystem-crossing-driven ladderdiene ring opening†

Zhendong Li,^a Haijun Fu,^{ab} Steven A. Lopez^{id} ^{*c} and Jingbai Li^{id} ^{*a}

Photochemical ring-opening reactions have become an essential tool for chemical syntheses under mild conditions with high atom economy. We propose a near-visible light-induced electrocyclic ring-opening reaction to afford cyclooctatetraene (COT) using carbonyl-functionalized tricyclooctadiene (**1**) based on our machine learning (ML) accelerated photodynamics simulations. Our CAM-B3LYP/cc-pVDZ calculations show that carbonyl group reduce the S_1 -energy of **1** to 3.65 eV (340 nm) from 6.25 eV, approaching the visible light range. The multiconfigurational CASSCF(12,11)/ANO-RCC-VDZP calculations show small S_1 and T_1 energy gaps near an S_1 -minimum region. Our ML-photodynamics simulations with 1000 FSSH trajectories revealed a stepwise ring-opening mechanism of **1** from the S_1 , dominated by relatively fast S_1/T_1 intersystem crossings in 20 ps. The trajectories predict that the quantum yield to carbonyl-functionalized COT is 89%, suggesting the light-induced ring-opening reaction of **1** is highly efficient. This work demonstrates a predictive ML-photodynamics application for photochemical reaction design.

Introduction

Cyclooctatetraene (COT) is an essential molecular framework with an eight-membered ring with four π_{CC} -bonds. The unique chemical structure of COT can access versatile chemical products *via* ring-closing and cycloaddition reactions, which have been widely used in natural product synthesis,^{1,2} drug design,³ and organic semiconductors.⁴ COT features a low-lying triplet state (1.03 eV),⁵ notable triplet absorption (350 nm),⁶ and a short triplet lifetime (100 μ s).⁶ Moreover, the triplet COT exhibits relatively low reactivity towards molecular oxygen. These features make COT an excellent triplet-state quencher for developing stable organic fluorophores⁷ and laser devices.⁸

The first synthesis of COT was reported in 1911 by Willstätter using pseudopelletierine (Fig. 1a).⁹ Later, many efforts have been made to improve the syntheses of COT and its derivatives with ethylene,¹⁰ butadiene,^{11,12} and cyclooctadiene¹³ (Fig. 1b). However, most strategies require transition metal catalysts (e.g., Ni,^{14–16} Cu,^{11,12} and Pb¹⁷) and extensive thermal energy and reaction time. Thus, a cost-efficient metal-free synthesis of COT

remains a challenging task. Photochemical reactions are gaining increasing importance in organic synthesis because of the mild reaction conditions,¹⁸ high atomic economy,¹⁹ and access to exotic molecular structures.²⁰ According to the literature, the photoexcitation of tricyclooctadiene (TOD) favors the electrocyclic ring-opening reactions toward COT.²¹ Our previous photodynamics studies on TOD showed the ring-opening of TOD occurs in the sub-picosecond timescale^{22,23} (Fig. 1c). Our simulations reproduced the trend of experimentally observed cubane yields depending on the substituent effects and explained the reaction pathway toward COT formation. Nevertheless, the lowest light absorption (S_1) is far beyond the visible range (198 nm) due to the transitions to the $\pi\pi^*$ states,²² which limit its applicability to produce COT.

Extending the π -conjugation of the vinyl groups with carbonyl groups to make α,β -unsaturated carbonyl compound can substantially reduce the energy S_1 state while maintaining the photochemical reactivity.^{24,25} A recent computational and experimental study showed self-sensitized photochemical dimerization of isophorone under visible-light irradiation.²⁴ These findings prompted us to envision a theoretical system featuring a carbonyl-functionalized TOD (Fig. 1d), **1** where visible light could promote the electrocyclic ring-opening reaction to generate a COT derivative (**4**). We are unaware of any experimental or computational studies investigating the photochemical reaction of **1**. It may result from time-resolved experiments that currently cannot resolve the structural information and inform the mechanism. Carbonyl compound are known to induce intersystem crossing during the excited-state

^aHoffmann Institute of Advanced Materials, Shenzhen Polytechnic University, 7098 Liuxian Blvd, Nanshan District, Shenzhen, 518055, People's Republic of China. E-mail: ljingbai@szpu.edu.cn

^bSchool of Chemistry and Chemical Engineering, Zhejiang Sci-Tech University, Hangzhou 310018, China

^cDepartment of Chemistry and Chemical Biology, Northeastern University, Boston, MA 02115, USA. E-mail: s.lopez@northeastern.edu

† Electronic supplementary information (ESI) available. See DOI: <https://doi.org/10.1039/d4sc07395a>



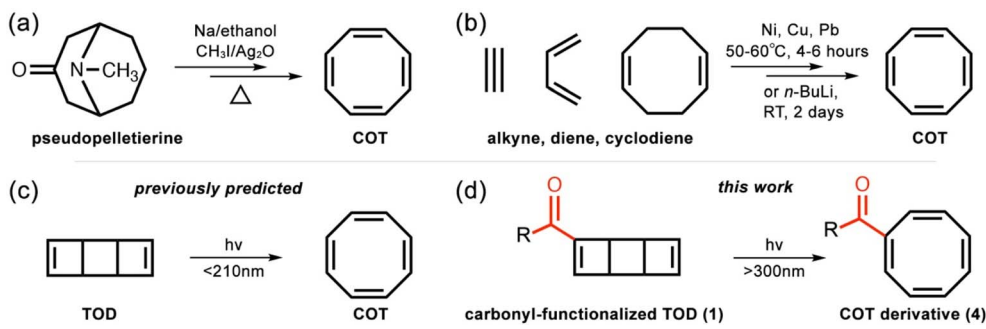


Fig. 1 (a) Synthesis of COT via elimination reactions of pseudopelletierine by Willstätter. (b) Synthesis of COT with transition metal-catalyzed thermal cycloaddition of alkene, dienes, and oxidation of cyclodiene. (c) Previously predicted photochemical 4 π -disrotatory electrocyclic ring-opening of TOD toward COT. (d) Proposed photochemical ring-opening of the carbonyl-functionalized TOD (1).

dynamics,^{26,27} which can extend the excited-state lifetime from tens to hundreds of picoseconds. The requisite multi-configurational quantum mechanical calculations are computationally infeasible for the 10–100 s of picoseconds, even for a relatively small molecule like **1**.

In this work, we combine the quantum mechanical calculations and machine learning (ML)-accelerated photodynamics approach to study the photochemical reactions of **1**. We first computed the vertical excitation energy of **1** with the time-dependent density functional theory (TDDFT) and complete active space self-consistent field (CASSCF) methods. We then train neural networks (NN) based on the ground- and excited-state CASSCF energies and gradients to simulate the excited-state dynamics of **1** starting from the S₁-Franck Condon (FC) regions. The discussion section analyzes the trajectories of possible excited-state mechanistic pathways of **1**. This manuscript aims to demonstrate a promising photochemical electrocyclic ring-opening reaction of **1** for the cost-efficient and metal-free synthesis of COT under mild conditions.

Results and discussion

Vertical excitation

The previous study reported the lowest absorption of the unsubstituted tricyclooctadiene (TOD) at 6.25 eV (198 nm), requiring ultraviolet light for photoexcitation.²² Towards a more chemoselective and sustainable methodology towards COT, we

introduce a carbonyl group to modulate the photophysical properties of **TOD**. Here, we used the aldehyde group as smallest carbonyl functional group to reduce the computational cost. Table 1 summarizes the vertical excitation energies and oscillator strength of **1** computed by various methods.

The CAM-B3LYP/cc-pVDZ calculations show the S₁, S₂, and S₃ energies of **1** are 3.65, 5.14 and 5.58 eV, respectively. These results indicate the carbonyl group substantially lowers the S₁ energy of **1** (3.65–3.70 eV) compared to **TOD** (6.25 eV).²² The S₁ of **1** is a n π^* state governed by the electronic transition from the oxygen lone pair of the carbonyl group to the lowest unoccupied π^* -orbital of **1** (Fig. S1†). The computed oscillator strengths (0.0006–0.0008) imply a low-intensity absorption to the S₁ of **1** upon photoexcitation near the visible light (340 nm). The S₂ and S₃ are $\pi\pi^*$ and $\sigma\pi^*$ states with larger absorption intensities and oscillator strengths than S₁, but photoexcitation to S₂ or S₃ requires UV light. Including diffuse functions in the double-zeta basis set (CAM-B3LYP/aug-cc-pVDZ) shows similar excitation energies, 3.68, 4.99, and 5.40 eV, respectively. Triple-zeta basis sets (*i.e.*, CAM-B3LYP/cc-pVTZ) do not significantly affect the vertical excitation energies and characters of S₁, S₂, and S₃ (3.70, 5.05, and 5.47 eV, respectively).

The triplet calculations at the CAM-B3LYP/cc-pVDZ level show nearly degenerate T_{1–3} states, where the T₁, T₂, and T₃ states are 2.87, 3.03, and 3.74 eV above S₀, respectively. The T₁ is a n π^* state, T₂ and T₃ are $\pi\pi^*$. The diffuse functions led to no significant effects on the triplet state energies and characters.

Table 1 The vertical excitation energies oscillator strength of **1** using different computational methods^a

Methods	Energy (eV)						Oscillator strength		
	S ₁	S ₂	S ₃	T ₁	T ₂	T ₃	S ₁	S ₂	S ₃
CAM-B3LYP/cc-pVDZ	3.65 (n π^*)	5.14 ($\pi\pi^*$)	5.58 ($\sigma\pi^*$)	2.87 (n π^*)	3.03 ($\pi\pi^*$)	3.74 ($\pi\pi^*$)	0.0006	0.0344	0.1171
CAM-B3LYP/aug-cc-pVDZ	3.68 (n π^*)	4.99 ($\pi\pi^*$)	5.40 ($\sigma\pi^*$)	2.87 (n π^*)	3.09 ($\pi\pi^*$)	3.73 ($\pi\pi^*$)	0.0009	0.0384	0.1313
CAM-B3LYP/cc-pVTZ	3.70 (n π^*)	5.05 ($\pi\pi^*$)	5.47 ($\sigma\pi^*$)	2.87 (n π^*)	3.10 ($\pi\pi^*$)	3.73 ($\pi\pi^*$)	0.0008	0.0355	0.1252
CASSCF(12,11)/ANO-RCC-VDZP	3.60 (n π^*)	6.92 (n π^* + $\pi\pi^*$)	7.45 ($\pi\pi^*$)	3.40 (n π^*)	3.55 ($\pi\pi^*$)	4.26 ($\pi\pi^*$)	0.00002	0.0020	0.0394
CASSCF(12,11)/ANO-RCC-VTZP	3.54 (n π^*)	6.86 (n π^* + $\pi\pi^*$)	7.40 ($\pi\pi^*$)	3.36 (n π^*)	3.52 ($\pi\pi^*$)	4.25 ($\pi\pi^*$)	0.00004	0.0017	0.0309
CASPT2 (12,11)/ANO-RCC-VDZP	3.78 (n π^*)	7.03 ($\pi\pi^*$) ²	7.48 ($\pi\pi^*$) ²	3.47 (n π^*)	3.74 ($\pi\pi^*$)	4.45 ($\pi\pi^*$)	0.00002	0.0021	0.0396
XMS-CASPT2 (12,11)/ANO-RCC-VDZP	4.01 (n π^*)	7.34 ($\pi\pi^*$) ²	7.61 ($\pi\pi^*$) ²	3.64 (n π^*)	3.92 ($\pi\pi^*$)	4.54 ($\pi\pi^*$)	0.00003	0.0065	0.0360

^a The dominant electronic configurations are labelled in the parenthesis.



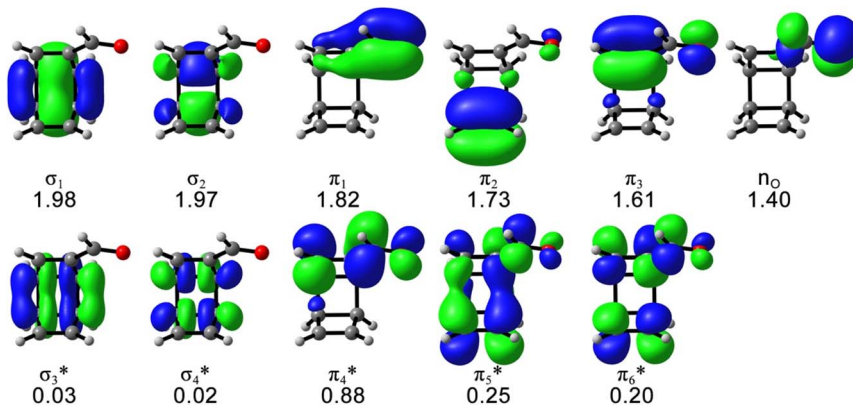


Fig. 2 The (12,11) active space of **1** with the average occupation numbers, computed at SA5-CASSCF(12,11)/ANO-RCC-VDZP level of theory. Isosurface value = 0.04.

The calculations with the cc-pVTZ basis set reproduced the similar results as cc-pVDZ. The small S_1 -T₁ and S_1 -T₂ gaps suggest that intersystem crossings are possible after direct photoexcitation to the FC-region.

We compared the CAM-B3LYP and ω B97X-D3 results to determine the influence of the chosen functionals on excited-state electronic structure calculations. Table S1† shows that ω B97X-D3 predicted systematically higher excited-state energies than CAM-B3LYP, which are 0.05–0.12 eV for S_1 , T₁, and T₂ and 0.22–0.36 eV for S_2 and S_3 . Despite the disagreement in excited-state energies and oscillator strengths, CAM-B3LYP and ω B97X-D3 produced the same electronic transitions in all singlet and triplet excited states (Table S2†). Thus, the CAM-B3LYP/cc-pVDZ results continue to guide our assembly of an active space for subsequent CASSCF calculations.

The possible electrocyclic ring-opening reactions of **1** after the photoexcitation to S_1 could lead to bond-breaking, which requires multiconfigurational descriptions of the potential energy surface and possible state-crossing regions. Thus, we employed the CASSCF calculations to study the excited-state relaxation of **1** from the S_1 -FC point toward **4**, including the

singlet internal conversion and the singlet-triplet intersystem crossing mechanistic pathways. The active space includes 12 electrons and 11 orbitals that describe all electrons involved in the electronic excitation according to the CAM-B3LYP/cc-pVDZ calculations and the essential electrons and orbitals participating in the photochemical reactions, as shown in Fig. 2.

The S_1 energy (3.60 eV) and electronic configuration of the 5-state-averaged (SA5)-CASSCF(12,11)/ANO-RCC-VDZP calculations agree with CAM-B3LYP/cc-pVDZ reference calculations (3.65 eV). The S_2 and S_3 energies are higher than the CAM-B3LYP/cc-pVDZ energies (6.92 and 7.45 eV, respectively) because the S_2 changed to a mix of $n\pi^*$ and $\pi\pi^*$ state and the S_3 includes double excitations in the SA5-CASSCF(12,11)/ANO-RCC-VDZP calculations. The oscillator strengths of S_{1-3} at the CASSCF(12,11)/ANO-RCC-VDZP level show the same trend as the CAM-B3LYP/cc-pVDZ results. The T₁₋₃ energies from the SA5-CASSCF(12,11)/ANO-RCC-VDZP calculations are 3.40, 3.55, and 4.26 eV, respectively, which are systematically higher than the results of the CAM-B3LYP/cc-pVDZ calculations while the electronic configurations are consistent with the CAM-B3LYP/cc-pVDZ results (Table 1). We tested a larger basis set (ANO-

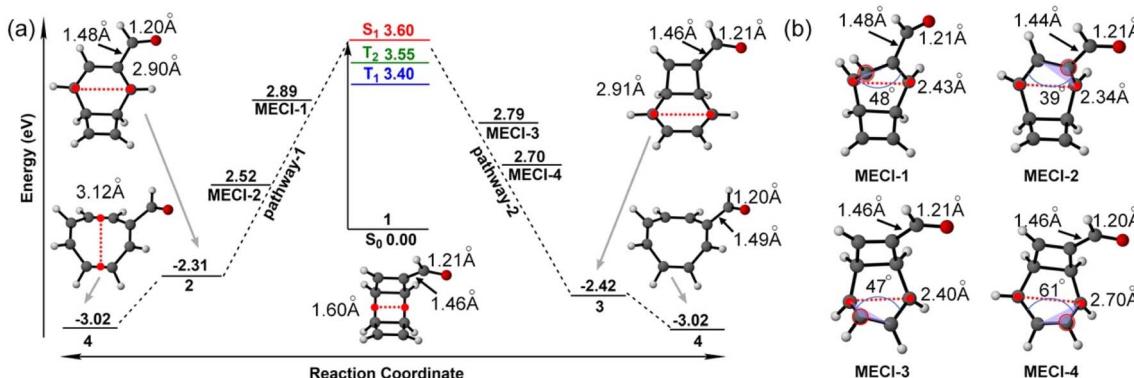


Fig. 3 (a) Potential energy profiles for the critical structures along with two electrocyclic ring-opening pathways at the SA5-CASSCF(12,11)/ANO-RCC-VDZP level. The red dotted lines show the breaking σ_{CC} bonds. (b) Optimized structures of MECIs. The red circles highlight the pyramidalized carbon, and the blue arches show the dihedral angles of over four connected carbon atoms. The lengths of breaking σ_{CC} bonds, substitution σ_{CC} bond, and π_{CO} bonds are labelled accordingly.



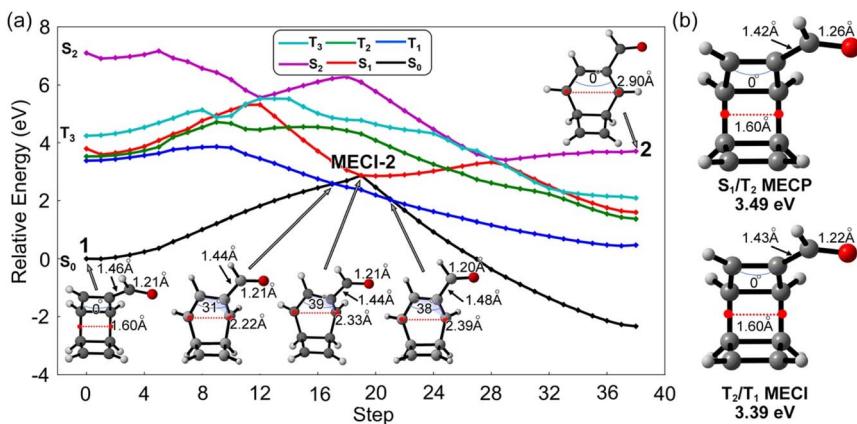


Fig. 4 (a) Interpolated reaction pathway for the first ring-opening step of **1**, computed at SA5-CASSCF(12,11)/ANO-RCC-VDZP level. The blue arches show the dihedral angles of over four connected carbon atoms. (b) Optimized structures of the S_1/T_2 and T_2/T_1 minimum energy crossing points (MECP) with the relative energies computed at the SA5-CASSCF(12,11)/ANO-RCC-VDZP level.

RCC-VTZP); it does not change the results but substantially increases the computation cost by 6 times.

To verify the accuracy of the CASSCF results, we employed the state-specific and extended multistate (XMS)-CASPT2 (12,11)/ANO-RCC-VDZP calculations, which partially account for dynamical correlation. Both calculations show similar S_1 energies to the SA5-CASSCF(12,11)/ANO-RCC-VDZP results, confirming the $n\pi^*$ character. However, the S_2 and S_3 states show $(\pi\pi^*)^2$ double excitations. Since TDDFT calculations cannot describe double excitations, it could result in discrepancies in the S_2 and S_3 energies compared to the CASPT2 and XMS-CASPT2 calculations. Nevertheless, the CASPT2(12,11)/ANO-RCC-VDZP and XMS-CASPT2(12,11)/ANO-RCC-VDZP calculations confirmed the relatively large S_1-S_2 and S_1-S_3 gaps (>3.0 eV) and the trends of their oscillator strengths observed in the SA5-CASSCF(12,11)/ANO-RCC-VDZP calculations. These results are in line with the CAM-B3LYP/cc-pVQZ results (1.49 eV), which avoid S_1 state crossing with S_2 and S_3 , especially in the FC region. The T_{1-3} states computed with the CASPT2(12,11)/ANO-RCC-VDZP and XMS-CASPT2(12,11)/ANO-RCC-VDZP calculations show similar energies and consistent electronic configurations to the SA5-CASSCF(12,11)/ANO-RCC-VDZP and CAM-B3LYP/cc-pVQZ results (Table 1). Moreover, we benchmarked the spin-orbit couplings (SOC) between S_0 , S_1 ,

T_1 , and T_2 (Table S4†). The SA5-CASSCF(12,11) calculations with the ANO-RCC-VDZP and ANO-RCC-VTZP basis sets show small differences of about 1 cm^{-1} in the SOC norms. The SA5-CASSCF(12,11)/ANO-RCC-VDZP results are consistent with the CAM-B3LYP/ZORA-TZVP calculations, including the zero-order relativistic effect. Thus, the SA5-CASSCF(12,11)/ANO-RCC-VDZP calculations are suitable for studying the photochemical reactions from the low-lying S_1 state with the neighboring triplet states.

Ring-opening pathways

Our previous work showed the electrocyclic ring-opening reaction of **TOD** starts from a 4π -disrotatory ring-opening process of the cyclobutene ring.²² We anticipate two competing reaction pathways at the carbonyl-functionalized cyclobutene ring or the unsubstituted terminus of **1**. Each ring-opening pathway goes through three mechanistic critical points from the S_1 -FC point to an S_1/S_0 minimum energy conical intersection (MECI) towards the product. We computed the energy profiles of these critical structures in these two pathways using the SA5-CASSCF(12,11)/ANO-RCC-VDZP method to understand the ring-opening mechanism. The optimized structures and relative energies are collected in Fig. 3.

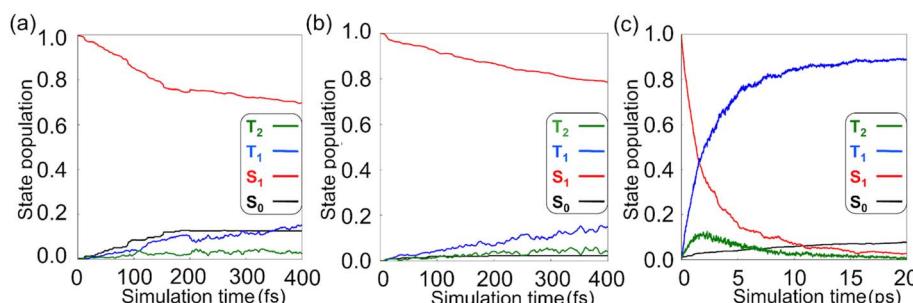


Fig. 5 (a) The state population dynamics of **1** in 400 fs nonadiabatic molecular dynamics with the SA5-CASSCF(12,11)/ANO-RCC-VDZP calculations. (b and c) The state population dynamics of **1** in the first 400 fs and 20 ps of the ML-photodynamics simulations.

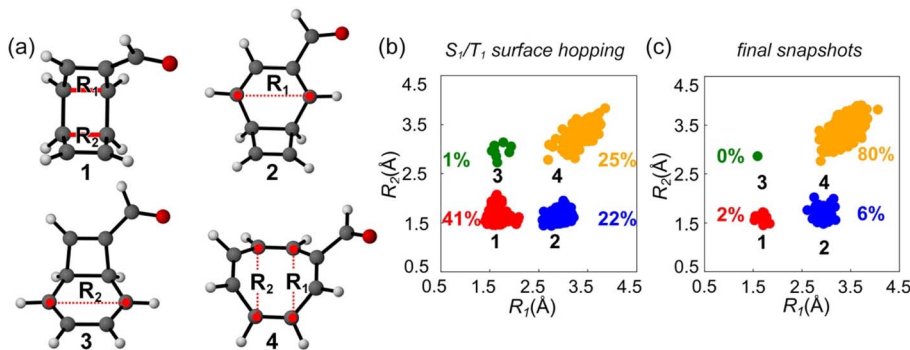


Fig. 6 (a) Illustration of the σ_{CC} bonds R_1 and R_2 in 1–4. The scatter plots for the structural distributions of (b) the latest S_1/T_1 surface hopping points and (c) the final snapshots via the $S_1 \rightarrow T_1$ transition in the ML-photodynamics simulations. The 2D space is defined by R_1 and R_2 .

We define the reaction coordinate as the midpoint of the σ_{CC} bonds that undergo electrocyclic ring opening reactions. The electrocyclic ring-opening of **1** elongates along the reaction coordinate from 1.60 Å to 2.90 Å and 2.91 Å in two isomers (**2** and **3**) of the carbonyl-functionalized bicyclooctatriene (**BOT**) and to 3.02 Å in the product **4** (Fig. 3a). **3** is more stable than **2** because of its shorter σ_{CC} bond lengths to the carbonyl groups, which lowers the energy *via* stronger π -electron delocalization.

The notable negative relative energies of **2**, **3** and **4** indicate the ring-opening process of **1** is thermodynamically favored on the ground state, which provides the driving force for the ring-opening reactions.

We located two possible MECIs for each pathway. **MECI-1** and **MECI-2** show the breaking σ_{CC} bonds of 2.43 Å and 2.34 Å with dihedral angles of the π_{CC} bond with the carbonyl group, 48° and 39°, respectively; **MECI-3** and **MECI-4** show the

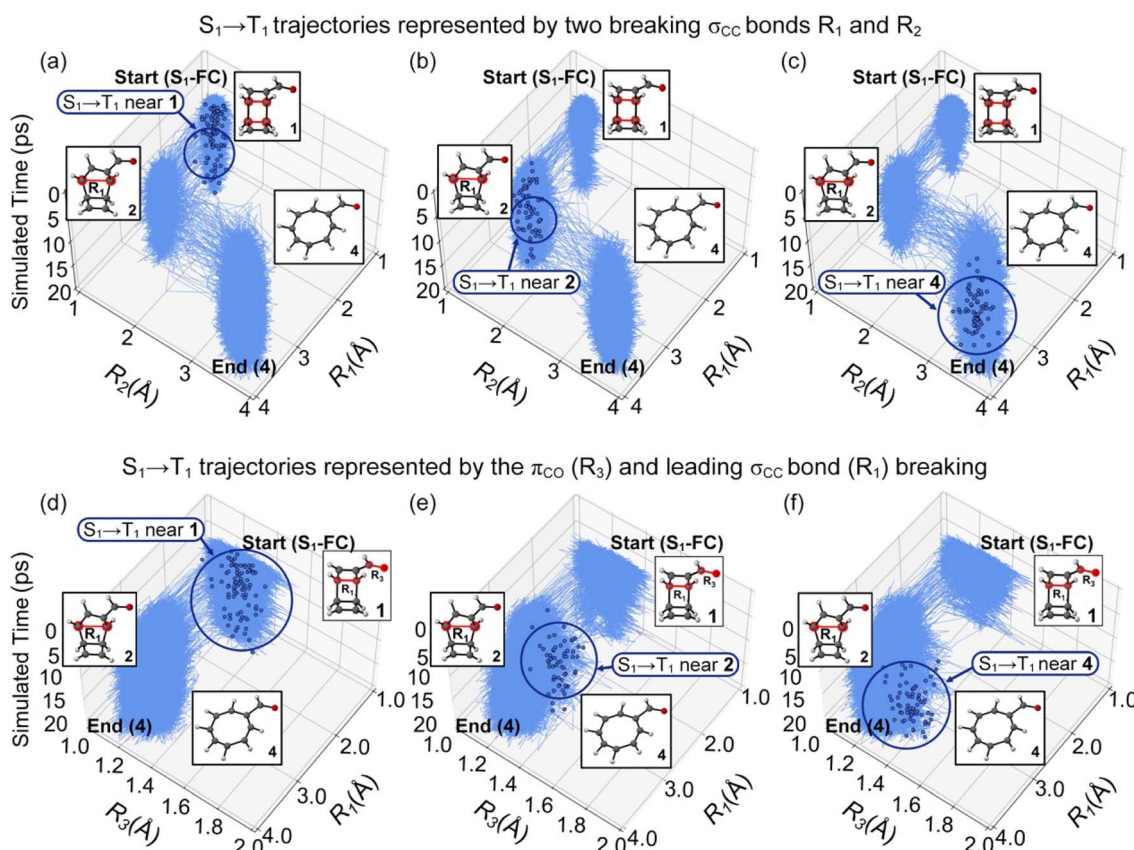


Fig. 7 Plots for the randomly selected trajectories in the 20 ps ML-photodynamics simulations. Three top panels plot the trajectories undergoing the S_1/T_1 intersystem crossings at regions (a) **1**, (b) **2**, and (c) **4** in a space defined by intramolecular distance R_1 and R_2 . Three bottom panels plot the trajectories undergoing the S_1/T_1 intersystem crossings at regions (d) **1**, (e) **2**, and (f) **4** in a space defined by the intramolecular distance R_1 and the π_{CO} bond distance R_3 . The blue dots represent the latest S_1/T_1 surface hopping points in trajectories. The dark blue circles highlight the locations of the S_1/T_1 surface hopping regions.



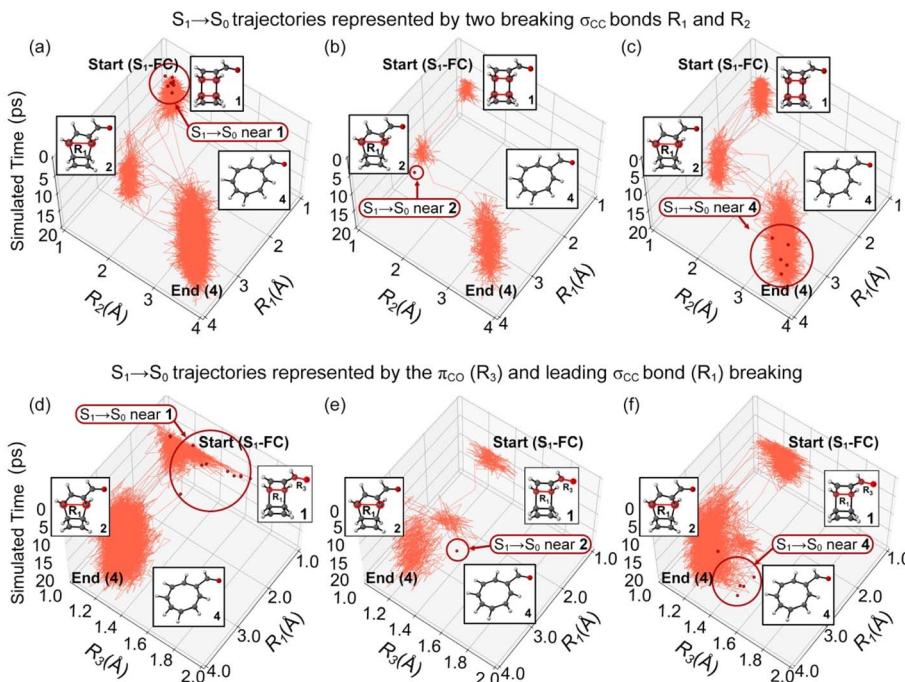


Fig. 8 Plots for the randomly selected trajectories in the 20 ps ML-photodynamics simulations. Three top panels plot the trajectories undergoing the S_1/S_0 surface hoppings at regions (a) 1, (b) 2, and (c) 4 in a space defined by the intramolecular distance R_1 and R_2 . Three bottom panels plot the trajectories undergoing the S_1/S_0 surface hoppings at regions (d) 1, (e) 2, and (f) 4 in a space defined by intramolecular distance R_1 and the π_{CC} bond distance R_3 . The red dots represent the latest S_1/S_0 surface hopping points in trajectories. The dark red circles highlight the locations of the S_1/S_0 surface hopping regions.

breaking σ_{CC} bonds of 2.40 Å and 2.70 Å with dihedral angles of 47° and 61° on the other π_{CC} bond, respectively (Fig. 3b). The MECIs feature σ_{CC} bond lengths that lengthen with larger dihedral angles on the π_{CC} bonds. These dihedral angles resemble the pyramidalization of the carbon atoms in the S_1/S_0 conical intersection of the *cis-trans* isomerization of the ethylene.²⁸ MECI-1 show a slightly longer σ_{CC} bond with the

carbonyl group (1.48 Å) than MECI-2 (1.44 Å), while the MECI-3 and MECI-4 show similar bonds of 1.46 Å due to the similar cyclobutene moieties. The π_{CO} bond distance is nearly identical (1.20–1.21 Å) in all involved structures. The MECI energies show a trend of MECI-1 (2.89 eV) > MECI-3 (2.79 eV) > MECI-4 (2.70 eV) > MECI-2 (2.52 eV). We note that the energetic trends do not correlate to the geometrical changes of the π_{CC} bond but relate

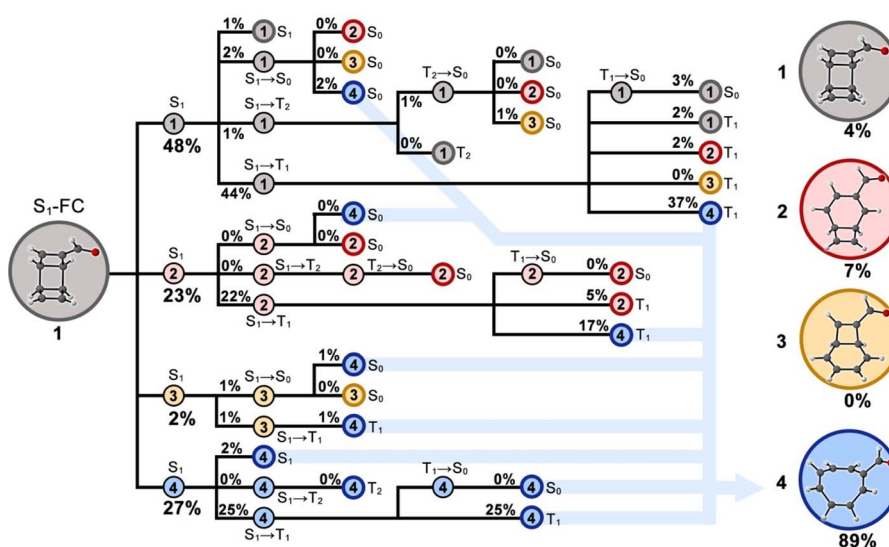


Fig. 9 Reaction network diagram for the photochemical electrocyclic ring-opening reaction of 1. The nodes with thin black circles correspond to the intermediate species, and the terminal nodes with bold-colored circles are products 1 (gray), 2 (pink), 3 (brown), and 4 (blue). The yields less than 1% are labelled with 0%. The blue arrows indicate the sources of product 4.

to the substitution σ_{CC} bond lengths. A possible explanation is that the shortened distance to the carbonyl groups could stabilize the diradicals *via* the extended delocalization, thus lowering the MECI energy. The energetic proximity of these MECIs suggests that multiple competing mechanistic pathways may exist.

The S_1 -FC (3.60 eV) energy is nearly degenerate with T_2 (3.55 eV) and T_1 (3.40 eV) (Fig. 3a). These results prompted us to investigate S_1/T_1 and S_1/T_2 intersystem crossing mechanisms in **1**. We interpolated the ring-opening pathways from the S_1 -FC to the **BOT** intermediates to inform the energetic relationship between the singlet and triplet states. Fig. 4a illustrates a representative potential energy curve for the three lowest singlet and triplet states from **1** to **2** *via* **MECI-2**. The potential energy curves for other pathways show similar topology, as shown in Fig. S3.[†]

The interpolated structures in Fig. 4a show continuous elongations along the reaction coordinate from **1** (1.60 Å) to **2** (2.90 Å). The maximum dihedral angle of the π_{CC} bond at the **MECI-2** structure is 39°. The S_1 state shows substantially smaller gaps to T_1 and T_2 than S_2 and T_3 in the first 5 steps, suggesting the T_1 and T_2 states are more mechanistically relevant to the ring-opening reaction of **1** than the S_2 and T_3 states. An S_1 minimum was located near the S_1 -FC point and is connected to **MECI-2** through an excited-state transition structure. The increasing S_1 energy could slow the $S_1 \rightarrow S_0$ transition *via* **MECI-2**. On the other hand, the depth of the S_1 -minimum combined with the small S_1/T_1 and S_1/T_2 energy gaps could promote the intersystem crossing. The nearly degenerate T_1 and T_2 states in the S_1 minimum region could also generate the T_2/T_1 internal conversion to enhance the T_1 population. The geometry optimizations for the four interpolated pathways led to the same S_1/T_2 and T_2/T_1 minimum energy crossing points (MECPs). The S_1/T_2 MECP structure shows increased π_{CO} bond length (1.26 Å) and reduced length of the substitution σ_{CC} bond (1.42 Å), while the T_2/T_1 MECI shows a nearly identical structure to the S_0 minimum geometry (Fig. 4b). The relative energies of the S_1/T_2 and T_2/T_1 crossings are 3.49 eV and 3.39 eV above the S_0 minimum and under the S_1 -FC point. These results suggest the intersystem crossing the subsequent triplet internal conversions is energetically favored. The T_1 state shows a relatively flat potential energy near the S_1 barrier, which requires less energy than S_1 and T_2 to afford the ring opening of **1**. The interpolated T_1 barriers are 0.48 eV, 0.42 eV, 0.95 eV, and 0.84 eV in pathways 1–4, respectively (Fig. S3[†]), which are confirmed by the energy profiles at the XMS-CASPT2(12,11)/ANO-RCC-VDZP level. These results indicate pathway 2 could be the most favored reaction channel. Despite the mechanistic hints provided by this static approach, only non-adiabatic molecular dynamics can provide answers to the hypotheses stated here.

Machine-learning photodynamic

To quantify the light-induced electrocyclic ring-opening mechanism for **1**, we enumerated all possible reaction pathways from the S_1 -FC regions using nonadiabatic molecular dynamics simulations based on the SA5-CASSCF(12,11)/ANO-RCC-VDZP

calculations. The simulated absorption spectrum shows notable bands in 300–400 nm because the vibronic coupling enhances the transition dipole moment of the $n\pi^*$ state, suggesting the S_1 of **1** is accessible for photoexcitation (Fig. S4[†]). As such, our simulations started from the S_1 -FC regions, where the initial conditions are generated by Wigner sampling at the zero-point energy level. We included S_0 , S_1 , T_1 , and T_2 because they are involved in the ring-opening reaction of **1**, according to the potential energy profile (Fig. 4). We employed the generalized fewest switches surface hopping (FSSH) method to evaluate the probability of the internal conversions and intersystem crossings.²⁹ The nonadiabatic couplings (NACs) are computed by the curvature-driven time derivative coupling (*k*TDC) approach.^{30,31} The SOCs are computed with the SA5-CASSCF(12,11)/ANO-RCC-VDZP calculations. Due to the high computational cost (*e.g.*, 4 days for a single trajectory), we propagated 300 trajectories in 400 fs with a time step of 0.5 fs.

We used our open-source ML-photodynamics code Python Rapid Artificial Intelligence *Ab Initio* Molecular Dynamics (PyRAI²MD) to train neural networks and accelerate the CASSCF calculations of the energies, gradients, and SOCs for the considered states. The ML-photodynamic simulations allowed us to propagate about 1000 trajectories in 20 ps with a timestep of 0.5 fs at substantially reduced computational costs (*e.g.*, 16 minutes for a single trajectory instead of 200 days with SA5-CASSCF(12,11)/ANO-RCC-VDZP calculations). The NN training employed adaptive sampling to iteratively collect undersampled data, where the unphysical structures with large energy outliers were discarded. 9% of the NN trajectories early stopped in the excited-state due to large NN prediction uncertainty, and thus are not included in subsequent discussions. The CASSCF- and NN-trajectories show similar energy conservation behavior. They maintained a small average energy drift of 0.08 and 0.01 eV, and gradually increased to 0.31 and 0.15 eV after multiple surface hoppings between discontinuous potential energy surfaces, which could be improved with reduced simulation time step.

The CASSCF state populations plot in Fig. 5a shows that 69% of trajectories remained in S_1 , while the S_0 and T_1 populations increased to 12% and 16%, respectively. The large remaining S_1 population suggests the reaction pathways from the S_1 -FC region are still largely unexplored. The NN-trajectories show comparable state populations to the SA5-CASSCF(12,11)/ANO-RCC-VDZP reference results (Fig. 5b). The S_1 population reduced to 79% while the T_1 population increased to 15%. It fits an S_1/T_1 intersystem crossing time constant of 1.7 ps, which is close to 2.0 ps obtained from the CASSCF reference trajectories. We note the NN-predicted trajectories of the $S_1 \rightarrow S_0$ transitions are 2%, which is lower than the reference trajectories (12%).

We performed an error analysis to further determine the origin of the discrepancy between the reference and NN-predicted trajectories and possible influence on the simulations results. Fig. S5[†] collects the NN-predicted energies and gradients for all MECIs. The S_0 and S_1 of **MECI-1**, **MECI-2**, and **MECI-3** show notable errors larger than 0.10 eV. As such, the enlarged out-of-sample prediction errors could lead to inaccurate population transfer from S_1 to S_0 , resulting in an



underestimated S_0 population in the dynamics. To determine the influence of underestimated $S_1 \rightarrow S_0$ transitions on the reaction channels, we turned off surface hopping (*i.e.*, infinitely slow intersystem crossing) and still observed the ring-opening reaction of **1** (Table S7†). This test suggests the ring-opening reaction of **1** is not sensitive to the underestimation of $S_1 \rightarrow S_0$ transitions.

Moreover, we prepared an out-of-sample test set based on the S_1/T_1 surface hopping structures collected from the ML-photodynamics trajectories to inform the NN prediction accuracy for out-of-sample structures far from the equilibrium geometries. Table S8† shows that the test errors in energies, gradients, and SOC norms are 5, 2, and 6 times the validation errors. In contrast to the narrow error distributions of energies and gradients, the SOC norms show a wide error distribution from -60 to 60 cm^{-1} with an MAE of 13.4160 cm^{-1} . To determine the sensitivity of ring-opening reaction to the ISC dynamics, we compared the ML-photodynamics with a constant bias by adding and subtracting the MAE to the predicted SOC norm. The 20 ps state population dynamics with reduced SOC norms (Fig. S7b†) show almost identical results to those without modifications on SOC norms (Fig. S7a†), suggesting the NN overestimations of the SOC norms do not significantly affect the $S_1 \rightarrow T_1$ ISC rates. Increasing the predicted SOC norm mainly speeds up the $T_1 \rightarrow S_0$ ISC after 10 ps but has little effect on the $S_1 \rightarrow T_1$ ISC (Fig. S7c†). In all cases, the predicted yields of **4** are similar (Table S7†), suggesting a small influence of the NN prediction errors on the ring-opening reaction mechanism of **1**. Thus, the NN errors will not significantly change our results and discussions on the photochemical ring-opening reaction mechanism of **1**.

The NN-predicted state population dynamics in 20 ps show that 89% of the trajectories finished at the T_1 state; only 8% trajectories arrived to S_0 state *via* the $S_1 \rightarrow S_0$ (3%), $T_1 \rightarrow S_0$ (2%), $T_2 \rightarrow S_0$ (3%) transitions (Fig. 5c). These results confirmed the S_1/T_1 intersystem crossing controls the S_1 non-radiative relaxation of **1**. We measured the σ_{CC} bond lengths in **1–4** to understand the structural changes during the $S_1 \rightarrow T_1$ transitions in the ML-photodynamics simulations (Fig. 6a).

The structural distributions in Fig. 6b show four clustering regions at the latest S_1/T_1 surface hopping points. 41% of trajectories at region **1** correspond to the trajectories hop to T_1 without breaking the σ_{CC} bonds. 22% of the trajectories undergo a 4π -disrotatory ring-opening at the carbonyl-functionalized cyclobutene ring at region **2**; 1% of the trajectories open the unsubstituted cyclobutene ring at region **3**. It suggests the carbonyl group facilitates the ring-opening reaction. Moreover, 25% of the trajectories at region **4** indicate the ring-opening reaction of two σ_{CC} bonds could also occur during the $S_1 \rightarrow T_1$ transitions. These results suggest that the ring-opening reactions are intrinsically favored in the S_1 and T_1 states of **1**.

Fig. 6c shows the final structural distributions of the trajectories undergoing the S_1/T_1 surface hoppings. The number of trajectories at regions **1–3** substantially decreased to 2%, 6%, and 0%, respectively. As a result, 80% of the trajectories arrived in region **4**. The trajectories forming **4** remained in T_1 after 20 ps

due to slow $T_1 \rightarrow S_0$ ISC. We considered them as final ground-state products since we did not observe any reverse reaction. The continuously increasing yield of **4** in our simulations suggests the second step ring-opening reaction of **1** is also thermodynamically favored.

The rare $S_1 \rightarrow S_0$ conical intersection and $T_n \rightarrow S_0$ intersystem crossings generally begin without breaking the σ_{CC} bonds of **1**. The trajectories undergoing the $S_1 \rightarrow S_0$ transitions directly afforded the ring-opening reaction. The trajectories in the $T_{1,2} \rightarrow S_0$ pathways first showed the above-mentioned $S_1 \rightarrow T_1$ or $S_1 \rightarrow T_2$ transitions and continued to hop to the ground state *via* the T_1/S_0 or T_2/S_0 intersections. These trajectories collectively contribute to another 7% of **4** on the ground state. In addition, we found 2% of **4** formed in the remaining S_1 trajectories. These results suggest even the minor reaction pathways favor the ring-opening reactions of **1**. Our ML photodynamics simulations predicted an overall 89% quantum yield of **4**.

We compared the NN-predicted trajectories in all possible reaction pathways to elucidate the ring-opening mechanisms of **1**. The trajectory plots in Fig. 7a–c illustrate the changes in the σ_{CC} bond lengths, R_1 and R_2 , as a function of simulation time.

Fig. 7a represents the trajectories undergoing the S_1/T_1 intersystem crossings near the S_1 -FC region at $R_1 = 1.62\text{ \AA}$ and $R_2 = 1.64\text{ \AA}$ (region **1**). After hopping to T_1 , these trajectories proceeded to the intermediate **2** at $R_1 = 2.92\text{ \AA}$ and $R_2 = 1.64\text{ \AA}$ and then the final product **4** at $R_1 = 3.34\text{ \AA}$, $R_2 = 3.31\text{ \AA}$, showing a stepwise ring-opening mechanism. Fig. 7b shows the first ring-opening step near the intermediate **2** before the $S_1 \rightarrow T_1$ transition. Then, the trajectories continued the second ring-opening step to form **4**. Fig. 7c highlights the trajectories formed **4** before the S_1/T_1 intersystem crossings. These results suggest a stepwise mechanism of the photochemical ring-opening reactions of **1** that first breaks the σ_{CC} bond in the ring substituted with the carbonyl groups and then breaks the other σ_{CC} bond. The S_1/T_1 intersystem crossings can occur at the S_1 -FC region, intermediate **2**, and product **4** indicates the σ_{CC} bond-breaking does not correlate with the S_1/T_1 intersystem crossing structures. We plot the π_{CO} bond distance (R_3) in the carbonyl group with R_1 in the trajectories (Fig. 7d–f) to determine the origin of the S_1/T_1 intersystem crossings. The average value of R_3 is 1.22 \AA at the S_1 -FC region. It notably increases to 1.31 \AA , 1.30 \AA , and 1.46 \AA at the S_1/T_1 intersystem crossing structures near the S_1 -FC (Fig. 7d), intermediate **2** (Fig. 7e), and product **4** regions (Fig. 7f), consistent with a partial triplet electronic structure. Thus, the elongation of the π_{CO} bond is responsible for the S_1/T_1 intersystem crossings during the photochemical ring-opening reaction of **1**.

The trajectories in Fig. 8a show the S_1/S_0 surface hopping structures near the S_1 -FC region ($R_1 = 1.66\text{ \AA}$ and $R_2 = 1.66\text{ \AA}$). Like the trajectories hoped to T_1 in Region **1** (Fig. 7a), these trajectories proceeded to a stepwise ring-opening reaction of **1** to form **4**. Fig. 8b illustrates the S_1 trajectories hoped to the ground state between the first and second steps of the ring-opening reaction of **1**. The S_1/S_0 surface hopping structures resemble MECI-2 with $R_1 = 3.14\text{ \AA}$, $R_2 = 1.66\text{ \AA}$. The second ring-opening step was completed in the ground state at product **4**, with $R_1 = 3.14\text{ \AA}$ and $R_2 = 3.30\text{ \AA}$ at the end of the simulations.



The trajectories directly formed **4** in S_1 are shown in Fig. 8c, and the trajectories still follow a stepwise ring-opening pathway. Similar to the S_1/T_1 intersystem crossings, we found increased π_{CO} bond lengths from 1.22 Å at the S_1 -FC regions to 1.58 Å, 1.54 Å, and 1.58 Å at the S_1/S_0 conical intersections near the S_1 -FC (Fig. 8d), intermediate **2** (Fig. 8e), and product **4** regions (Fig. 8f). These findings indicate the same ring-opening mechanism of **1** via the S_1/S_0 conical intersections and S_1/T_1 intersystem crossing but only differ in the time constants.

Combining the electronic state population distributions and structural classifications in the trajectories produces a comprehensive reaction network for the predicted photochemical electrocyclic ring-opening reaction of **1** toward **4** (Fig. 9). The detailed and quantitative connections over all reactant, intermediates, and products across multiple singlet and triplet states provide a deep understanding of the ring-opening mechanisms.

Conclusion

We combined the quantum mechanical calculations and machine learning photodynamics approach to enable long timescale photodynamics simulations for uncovering unexpected photochemical reaction pathways. Our showcase study on the stepwise ring-opening mechanisms of **1** show competing S_1/T_1 intersystem crossings and S_1/S_0 conical intersections, where the first ring-opening step starts at the carbonyl-functionalized cyclobutene ring. The CAM-B3LYP/cc-pVDZ calculations show that connecting to a carbonyl group substantially reduced the S_1 energy from 6.25 eV to 3.68 eV. The SA5-CASSCF(12,11)/ANO-RCC-VDZP calculations show a close S_1/T_1 gap (0.2 eV) in the S_1 -FC region along with the interpolated ring-opening reaction pathways. The 20 ps ML-photodynamics simulations show dominant S_1/T_1 intersystem crossings with a lifetime of 1.4 ps. The overall predicted quantum yield of **4** is 89%.

The trajectory analysis revealed a diverse reaction channel of the photochemical ring-opening reaction of **1** in S_1 and T_1 states. The ring-opening mechanism favors a stepwise σ_{CC} bond-breaking in **1**, where the cyclobutene substituted with the carbonyl group opens before the ring on the other side. Further characterizations of the trajectories show that the elongation of the π_{CO} bond length of the carbonyl groups generates the S_1/T_1 intersystem crossing and S_1/S_0 conical intersections. Thus, the photochemical ring-opening reaction of **1** is independent of whether it is in the S_1 or T_1 states. As such, the S_1 excitation energy became the main driving force to break the σ_{CC} bonds of **1**, which explains the high efficiency of the ring-opening reaction. Overall, our work demonstrates a feasible and light-controllable reaction tool for preparing the COT derivatives in a high yield.

Computational details

Quantum mechanical calculation

We optimized the gas-phase geometries of **1** using the density functional theory (DFT) at the PBE0/cc-pVDZ level. Frequency

calculations confirmed the local minimum with no imaginary frequencies. The vertical excitation energies and oscillator strengths were computed at the CAM-B3LYP/cc-pVDZ, CAM-B3LYP/aug-cc-pVDZ and CAM-B3LYP/cc-pVTZ levels using the time-dependent DFT (TD-DFT) theory. The (TD)DFT calculations were carried out by the BDF program.³²⁻³⁴ The SA5-CASSCF(12,11)/ANO-RCC-VDZP, CASPT2(12,11)/ANO-RCC-VDZP, and XMS-CASPT2(12,11)/ANO-RCC-VDZP calculations were performed with OpenMolcas.19.11.³⁵ The CAPST2 and XMS-CASPT2 used a level shift of 0.4 eV to avoid the intruder state problem.

Training data generation

The initial training data consists of two parts, generated by Wigner sampling and geometry interpolations. We first generate 20 non-equilibrium structures for **1** with the Wigner sampling at the zero-point energy level. Then, we collected 39 structures in the interpolated pathway from **1** to each MECI (Fig. S3†). Mixing the Wigner sampled and interpolated structures in all four pathways gave 3210 data points. The Wigner sampling uses the PyRAI²MD sampling tool,³⁶ the geometry interpolation uses the geodesic interpolation program.^{37,38} The training data contain the S_0 , S_1 , T_1 , and T_2 energies, gradients, and the norm of the spin-orbit couplings (SOCs) for S_1-T_2 , S_1-T_1 , S_0-T_2 , and S_0-T_1 , computed with the SA5-CASSCF(12,11)/ANO-RCC-VDZP calculations. We performed adaptive sampling to collect the under-sampled data points in the initial training data. Two independently trained NNs were used as a committee model. We used the potential model (*i.e.*, energies and gradients) together with the SOC model to propagate 100 trajectories from the S_1 -FC points in 10 ps with a step size of 0.5 fs. We used the standard deviations of NN-predicted energies, gradients, and SOC norms to measure the prediction uncertainty, which early stopped the trajectories when the prediction uncertainty exceeded the empirical thresholds (energy: 0.05 hartree; gradient: 0.25 hartree bohr⁻¹; SOC norm: 60 cm⁻¹). The final data size is 6459. Details about the adaptive sampling are available in Table S5.† All training data are computed with the SA5-CASSCF(12,11)/ANO-RCC-VDZP calculation.

Neural networks

We implemented a fully connected feedforward NNs using TensorFlow/Keras API for Python. The NN computes the inverse distance matrix of the input molecule to predict the energies, gradients, and SOC norms. The predicted energy gap between two singlet or triplet states is used to compute the curvature-approximated time derivative coupling (*kTDC*),^{30,31} derived from the Baeck-An approximation.³⁹ The NNs employ a leaky softplus activation function. The NNs used the first-order energy derivatives of atomic coordinates to fit the gradients, which ensures the physical relationship between energy and gradient. The energies and gradients of four electronic states are trained together with a combined loss function. Four NNs were trained simultaneously, where two NNs predict energy and gradient of four electronic states and two NNs predict SOC norms of four pairs of states. The training data are split into



training and validation sets in a 9 : 1 ratio. The final validation mean absolute errors (MAEs) for NN-predicted energies are 0.0337–0.0340 eV. Additional information about the NN training and error evaluation is available in ESI.†

ML-photodynamics simulations

We prepared the initial conditions for **1** by Wigner sampling at the zero-point energy level. The ML-photodynamics simulations were set to 20 ps with a timestep of 0.5 fs. The probability of a nonadiabatic electronic transition was computed with Tully's fewest switches surface hopping (FSSH) method^{40,41} using spin-diabatic representation, where the generalized formalism²⁹ was used to take the intersystem crossing into account. We used the curvature-approximated time-derivative coupling (*k*TDC) method^{30,31} to evaluate the nonadiabatic couplings based on the NN-predicted energies when the S₁–S₀ and T₂–T₁ gaps are smaller than 0.5 eV. The ML-photodynamics approach is implemented in PyRAI²MD.³⁶ The nuclear timestep is 0.5 fs and the electronic timestep is 0.025 fs corresponding to 20 substeps in the surface hopping calculations.

Data availability

The code for PyRAI2MD can be found at <https://github.com/mlcclab/PyRAI2MD-hiam>. The data supporting this article have been included as part of the ESI† and can be found at https://github.com/mlcclab/PyRAI2MD_publications/tree/main/triplet_COT.

Author contributions

Z. L. performed all calculations and prepared the first draft of the manuscript. Z. L. and J. L. analyzed the data. H. F. helped revise the manuscript. S. A. L. and J. L. conceived the idea of this work and revised the manuscript. J. L. oversaw the administration of this project.

Conflicts of interest

The authors declare no conflicts of interests.

Acknowledgements

J. L. acknowledges the funding support by the National Natural Science Foundation Grants (22303053). Z. L. and J. L. thank the support of the high-performance computing resources at Hoffmann Institute of Advanced Materials at Shenzhen Polytechnic University. Z. L. and J. L. gratefully acknowledge HZWTECH for providing computation facilities. S. A. L. acknowledges the NSF (NSF-CHE-2144556) for funding. J. L. and S. A. L. appreciate the assistance from the Northeastern Research Computing Team and the computing resources provided by the Massachusetts Life Science Center Grant (G00006360).

References

- L. Kelebekli, M. Çelik, E. Şahin, Y. Kara and M. Balci, Stereospecific synthesis of a new class of aminocyclitol with the conduramine D-2 configuration, *Tetrahedron Lett.*, 2006, **47**(39), 7031–7035.
- L. Kelebekli, Y. Kara and M. Balci, Stereospecific synthesis of a new class of compounds: bis-homoconduritol-A,-D, and-F, *Carbohydr. Res.*, 2005, **340**(12), 1940–1948.
- A. Xiong, G. Ma, K. Maeda, T. Takata, T. Hisatomi, T. Setoyama, J. Kubota and K. Domen, Fabrication of photocatalyst panels and the factors determining their activity for water splitting, *Catal. Sci. Technol.*, 2014, **4**(2), 325–328.
- T. Nishinaga, T. Ohmae, K. Aita, M. Takase, M. Iyoda, T. Arai and Y. Kunugi, Antiaromatic planar cyclooctatetraene: a strategy for developing ambipolar semiconductors for field effect transistors, *Chem. Commun.*, 2013, **49**(47), 5354–5356.
- A. K. Pati, O. El Bakouri, S. Jockusch, Z. Zhou, R. B. Altman, G. A. Fitzgerald, W. B. Asher, D. S. Terry, A. Borgia and M. D. Holsey, Tuning the Baird aromatic triplet-state energy of cyclooctatetraene to maximize the self-healing mechanism in organic fluorophores, *Proc. Natl. Acad. Sci. U. S. A.*, 2020, **117**(39), 24305–24315.
- T. NatháDas and K. IndiraÁPriyadarshini, Triplet of cyclooctatetraene: Reactivity and properties, *J. Chem. Soc., Faraday Trans.*, 1994, **90**(7), 963–968.
- Q. Zheng, S. Jockusch, Z. Zhou, R. B. Altman, J. D. Warren, N. J. Turro and S. C. Blanchard, On the mechanisms of cyanine fluorophore photostabilization, *J. Phys. Chem. Lett.*, 2012, **3**(16), 2200–2203.
- V. T. Mai, V. Ahmad, M. Mamada, T. Fukunaga, A. Shukla, J. Sobus, G. Krishnan, E. G. Moore, G. G. Andersson and C. Adachi, Solid cyclooctatetraene-based triplet quencher demonstrating excellent suppression of singlet–triplet annihilation in optical and electrical excitation, *Nat. Commun.*, 2020, **11**(1), 5623.
- R. Willstätter and E. Waser, Über Cyclo-octatetraen, *Ber. Dtsch. Chem. Ges.*, 1911, **44**(3), 3423–3445.
- J. H. Rigby and N. C. Warshakoon, A convenient synthesis of 1, 2-disubstituted cyclooctatetraenes, *Tetrahedron Lett.*, 1997, **38**(12), 2049–2052.
- C. Wang, J. Yuan, G. Li, Z. Wang, S. Zhang and Z. Xi, Metal-mediated efficient synthesis, structural characterization, and skeletal rearrangement of octasubstituted semibullvalenes, *J. Am. Chem. Soc.*, 2006, **128**(14), 4564–4565.
- Y. Yamamoto, T. Ohno and K. Itoh, Selective synthesis of fused cyclooctatetraenes by [4 + 4] coupling between two different diene units, *Chem.–Eur. J.*, 2002, **8**(20), 4734–4741.
- S. Majumder and A. L. Odom, Simple and convenient one-pot synthesis of cyclooctatetraene, *Tetrahedron Lett.*, 2008, **49**(11), 1771–1772.
- W. Reppe, O. Schlichting, K. Klager and T. Toepel, Cyclisierende Polymerisation von acetylen I über



cyclooctatetraen, *Justus Liebigs Ann. Chem.*, 1948, **560**(1), 1–92.

15 P. A. Wender, J. P. Christy, A. B. Lesser and M. T. Gieseler, The Synthesis of Highly Substituted Cyclooctatetraene Scaffolds by Metal-Catalyzed [2 + 2 + 2 + 2] Cycloadditions: Studies on Regioselectivity, Dynamic Properties, and Metal Chelation, *Angew. Chem., Int. Ed.*, 2009, **48**(41), 7687–7690.

16 P. A. Wender and J. P. Christy, Nickel (0)-catalyzed [2 + 2 + 2 + 2] cycloadditions of terminal diynes for the synthesis of substituted cyclooctatetraenes, *J. Am. Chem. Soc.*, 2007, **129**(44), 13402–13403.

17 S. Blouin, V. Gandon, G. Blond and J. Suffert, Synthesis of Cyclooctatetraenes through a Palladium-Catalyzed Cascade Reaction, *Angew. Chem., Int. Ed.*, 2016, **55**(25), 7208–7211.

18 J. Xuan, X.-K. He and W.-J. Xiao, Visible light-promoted ring-opening functionalization of three-membered carbo-and heterocycles, *Chem. Soc. Rev.*, 2020, **49**(9), 2546–2556.

19 Y. Zheng, W. Huang, R. K. Dhungana, A. Granados, S. Keess, M. Makvandi and G. A. Molander, Photochemical intermolecular [3σ+ 2σ]-cycloaddition for the construction of aminobicyclo [3.1. 1] heptanes, *J. Am. Chem. Soc.*, 2022, **144**(51), 23685–23690.

20 D. P. Poudel, A. Pokhrel, R. K. Tak, M. Shankar and R. Giri, Photosensitized O₂ enables intermolecular alkene cyclopropanation by active methylene compounds, *Science*, 2023, **381**(6657), 545–553.

21 R. Gleiter and S. Brand, Photochemistry of Bridged and Unbridged Octaalkyl-Substituted syn-Tricyclo [4.2. 0.02, 5] octa-3, 7-diene Derivatives, *Chem.-Eur. J.*, 1998, **4**(12), 2532–2538.

22 J. Li and S. A. Lopez, Multiconfigurational calculations and nonadiabatic molecular dynamics explain tricyclooctadiene photochemical chemoselectivity, *J. Phys. Chem. A*, 2020, **124**(38), 7623–7632.

23 J. Li, R. Stein, D. M. Adrián and S. A. Lopez, Machine-learning photodynamics simulations uncover the role of substituent effects on the photochemical formation of cubanes, *J. Am. Chem. Soc.*, 2021, **143**(48), 20166–20175.

24 J. Xie, X. Zhang, C. Shi, L. Pan, F. Hou, G. Nie, J. Xie, Q. Liu and J.-J. Zou, Self-photosensitized [2+ 2] cycloaddition for synthesis of high-energy-density fuels, *Sustainable Energy Fuels*, 2020, **4**(2), 911–920.

25 M. A. Theodoropoulou, N. F. Nikitas and C. G. Kokotos, Aldehydes as powerful initiators for photochemical transformations, *Beilstein J. Org. Chem.*, 2020, **16**(1), 833–857.

26 S. Maeda, K. Ohno and K. Morokuma, A theoretical study on the photodissociation of acetone: Insight into the slow intersystem crossing and exploration of nonadiabatic pathways to the ground state, *J. Phys. Chem. Lett.*, 2010, **1**(12), 1841–1845.

27 L. Favero, G. Granucci and M. Persico, Dynamics of acetone photodissociation: a surface hopping study, *Phys. Chem. Chem. Phys.*, 2013, **15**(47), 20651–20661.

28 B. G. Levine and T. J. Martínez, Isomerization through conical intersections, *Annu. Rev. Phys. Chem.*, 2007, **58**(1), 613–634.

29 G. Cui and W. Thiel, Generalized trajectory surface-hopping method for internal conversion and intersystem crossing, *J. Chem. Phys.*, 2014, **141**(12), 124101.

30 Y. Shu, L. Zhang, X. Chen, S. Sun, Y. Huang and D. G. Truhlar, Nonadiabatic dynamics algorithms with only potential energies and gradients: Curvature-driven coherent switching with decay of mixing and curvature-driven trajectory surface hopping, *J. Chem. Theory Comput.*, 2022, **18**(3), 1320–1328.

31 X. Zhao, I. C. Merritt, R. Lei, Y. Shu, D. Jacquemin, L. Zhang, X. Xu, M. Vacher and D. G. Truhlar, Nonadiabatic coupling in trajectory surface hopping: accurate time derivative couplings by the curvature-driven approximation, *J. Chem. Theory Comput.*, 2023, **19**(19), 6577–6588.

32 W. Liu, F. Wang and L. Li, Relativistic density functional theory: The BDF program package, *Recent advances in relativistic molecular theory*, 2004, pp. 257–282.

33 Y. Zhang, B. Suo, Z. Wang, N. Zhang, Z. Li, Y. Lei, W. Zou, J. Gao, D. Peng and Z. Pu, BDF: A relativistic electronic structure program package, *J. Chem. Phys.*, 2020, **152**(6), 064113.

34 W. Liu, F. Wang and L. Li, The Beijing density functional (BDF) program package: methodologies and applications, *J. Theor. Comput. Chem.*, 2003, **2**(02), 257–272.

35 I. Fdez Galván, M. Vacher, A. Alavi, C. Angeli, F. Aquilante, J. Autschbach, J. J. Bao, S. I. Bokarev, N. A. Bogdanov and R. K. Carlson, OpenMolcas: From source code to insight, *J. Chem. Theory Comput.*, 2019, **15**(11), 5925–5964.

36 J. Li, P. Reiser, B. R. Boswell, A. Eberhard, N. Z. Burns, P. Friederich and S. A. Lopez, Automatic discovery of photoisomerization mechanisms with nanosecond machine learning photodynamics simulations, *Chem. Sci.*, 2021, **12**(14), 5302–5314.

37 X. Zhu, K. C. Thompson and T. J. Martínez, Geodesic interpolation for reaction pathways, *J. Chem. Phys.*, 2019, **150**(16), 164103.

38 M. Abadi, A. Agarwal, P. Barham, E. Brevdo, Z. Chen, C. Citro, G. S. Corrado, A. Davis, J. Dean and M. Devin, Tensorflow: Large-scale machine learning on heterogeneous distributed systems, *arXiv*, 2016, preprint, arXiv:1603.04467, DOI: [10.48550/arXiv.1603.04467](https://doi.org/10.48550/arXiv.1603.04467).

39 K. K. Baeck and H. An, Practical approximation of the non-adiabatic coupling terms for same-symmetry interstate crossings by using adiabatic potential energies only, *J. Chem. Phys.*, 2017, **146**(6), 064107.

40 J. C. Tully, Molecular dynamics with electronic transitions, *J. Chem. Phys.*, 1990, **93**(2), 1061–1071.

41 S. Hammes-Schiffer and J. C. Tully, Proton transfer in solution: Molecular dynamics with quantum transitions, *J. Chem. Phys.*, 1994, **101**(6), 4657–4667.

